

Diffuse reflection boundary condition at the continuum limit and bounce-back boundary condition

Jianping Meng, Xiao-Jun Gu, and David R Emerson

Scientific Computing Department, STFC Daresbury Laboratory, Warrington WA4 4AD, United Kingdom

Yong Peng and Jianmin Zhang

State Key Laboratory of Hydraulics and Mountain River Engineering, Sichuan University, Chengdu, 610065, P. R. China

Abstract:

In this work, it is found that the widely used **bounce-back** (BB) boundary condition is an incomplete form of the **diffuse reflection** (DR) boundary condition at the continuum limit for lattice Boltzmann simulations. By utilizing this fact, we can force the DR scheme to work at its continuum limit so that the non-slip boundary condition can be implemented without the non-physical slip velocity error induced by the standard BB scheme. The devised boundary formulation is validated numerically by using the pressure driven channel flows, the lid-driven cavity flows and the channel flow around a square cylinder.

1. Introduction

For lattice Boltzmann (LB) simulations, it is of great importance to correctly implement non-slip wall boundary condition for wide range of flow problems. The **bounce-back** (BB) scheme is perhaps the most widely used one among various implementations. It is easy to apply and works particularly well with the cutting-cell mesh technique, i.e., a series of zig-zag stairs are used to approximate complex boundary curve or surface. The moving boundary can also be treated via a simple modification suggested in [1]. However, the BB scheme suffers the non-physical slip velocity generated at the wall, which is discussed in detail in [2,3]. This can induce simulation errors in flows with simple [4] and complex geometry, e.g., predicting permeability of porous medium [5,6]. In [7], it is found that the BB scheme misses the definition of certain discrete velocities and causes the non-physical slip velocity. To correctly implement the non-slip velocity boundary, it is important to supplement the missing definition. This is fairly easy for simple geometries but remains open for general flow problems. On the other hand, it is also worth noting that the BB scheme provides a complete definition if using a lattice without zero velocity component and the cutting-cell mesh technique, e.g., the D2Q4 lattice structure analysed in [7]. However, lattices with zero velocity component are more common in the literature [8,9].

Diffuse reflection (DR) boundary scheme (also known as the kinetic boundary scheme) is believed to be consistent with physical effects for modelling slip velocity at the wall [10]. Therefore, it is often employed together with the **discrete velocity model** (DVM) for rarefied gas flows (see e.g., [11]). As the LB method may be considered as a special form of DVM, the DR scheme was naturally introduced into the LB simulations [12]. While the boundary scheme can help the LB scheme to capture the rarefied gas effects to some extent [13,14], it is also assessed for the lid-driven cavity flows with high Reynold (Re) number and the produced slip velocity show negligible impacts on simulations [15]. It is because that the slip velocity

become negligible with increasing Reynold number and decreasing Knudsen (Kn) number. In the limit of $Kn \rightarrow 0$, the non-slip boundary will be fully recovered.

In this work, by investigating the limiting behavior at $Kn \rightarrow 0$ of the DR scheme, we find that the BB scheme is an incomplete form of the continuum limit of the DR scheme. Therefore, we are able to supplement the definition missed by the BB scheme, and correctly implement the non-slip velocity boundary in general. In the following, we will first briefly introduce the lattice Boltzmann model and two boundary conditions, and then analyze the relation between two boundary schemes. Based on the identified relation, we devise an **equilibrium diffuse reflection (EDR)** boundary scheme for implementing the non-slip boundary condition. Finally, we will validate the proposed boundary formulation by simulating the pressure-driven channel flow, the lid-driven cavity flow and the channel flow around a square cylinder.

2. Lattice Boltzmann model

The lattice Boltzmann model can be derived via various procedures, see, e.g., [16–18], and may be considered a special form of DVM [13,19]. Its governing equation can be written as

$$\frac{\partial f_\alpha}{\partial t} + \mathbf{C}_\alpha \cdot \frac{\partial f}{\partial \mathbf{r}} = \frac{1}{\tau} (f_\alpha^{eq} - f_\alpha), \quad (1)$$

which describes the evolution of the single-particle distribution function $f_\alpha(\mathbf{r}, t)$ for the α th discrete velocity $\mathbf{C}_\alpha = (c_x, c_y)$ at position $\mathbf{r} = (x, y)$ for two-dimensional flows. For simplicity, the particle interaction can be modeled using a relaxation term towards the discrete equilibrium distribution function $f_\alpha^{eq}(\mathbf{r}, t)$. For incompressible and isothermal flows, the Maxwellian distribution can often be truncated into a second order polynomial, i.e.,

$$f_\alpha^{eq} = \rho g_\alpha^{eq} = \rho w_\alpha \left\{ 1 + \frac{\mathbf{C}_\alpha \cdot \mathbf{V}}{\theta_0} + \frac{1}{2} \left[\frac{(\mathbf{C}_\alpha \cdot \mathbf{V})^2}{\theta_0^2} - \frac{\mathbf{V} \cdot \mathbf{V}}{\theta_0} \right] \right\}, \quad (2)$$

which is determined by the density, ρ , the fluid velocity, $\mathbf{V} = (u, v)$, and the reference temperature θ_0 . The relaxation time, τ , is related to the viscosity, μ , via the relation $\mu = p\tau$. The Reynold number and Knudsen number can also be defined accordingly, see [15] for details. Together with Eq. (2), a D2Q9 lattice model with nine discrete velocities

$$c_x = \sqrt{3\theta_0} (0, 1, 0, -1, 0, 1, -1, -1, 1), \quad (3)$$

and

$$c_y = \sqrt{3\theta_0} (0, 0, 1, 0, -1, 1, 1, -1, -1), \quad (4)$$

is often adopted, where the corresponding weights are

$$w = \left(\frac{4}{9}, \frac{1}{9}, \frac{1}{9}, \frac{1}{9}, \frac{1}{9}, \frac{1}{36}, \frac{1}{36}, \frac{1}{36}, \frac{1}{36} \right). \quad (5)$$

With the discretized model, the macroscopic fluid density and flow velocity can be obtained via

$$\rho = \sum_{\alpha=0}^8 f_\alpha \quad \rho \mathbf{V} = \sum_{\alpha=0}^8 f_\alpha \mathbf{c}_\alpha. \quad (6)$$

Eq. (1) can be numerically solved by using the scheme

$$f_\alpha(t + dt, \mathbf{r} + \mathbf{c}_\alpha dt) - f_\alpha(t, \mathbf{r}) = \frac{dt}{\tau + 0.5 dt} (f_\alpha^{eq} - f_\alpha), \quad (7)$$

which is able to achieve second order accuracy in both time and space [20].

3. Continuum limit of diffuse-reflection boundary condition

For convenience, we briefly give the definition of the DR scheme and the BB scheme for the D2Q9 lattice.

With the DR scheme, an outgoing particle completely forgets its history and its velocity is re-normalized by the Maxwellian distribution. Moreover, we also assume that the effective particle-wall interaction time is small in comparison to any characteristic time of interest and no permanent adsorption occurs. To write down the mathematical description, the discrete velocities are categorized into three types, i.e., **Incoming** (blue solid lines), **Outgoing** (red dashed lines), and **Parallel** (black dash-dot lines), see Figure 1.

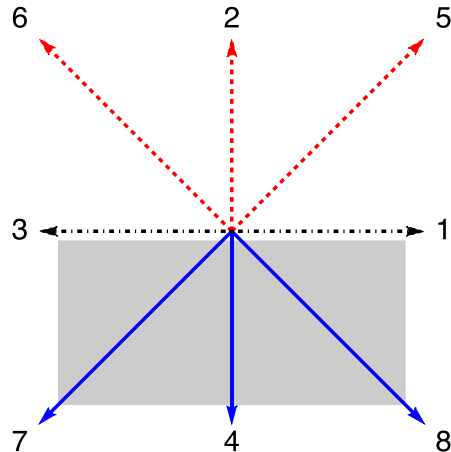


Figure 1 Schematic of a bottom wall boundary. Wall is illustrated by using gray shading.

For planar surface, its normal \mathbf{n} is often used to distinguish the three types of discrete velocities e.g., $\alpha \in \mathbf{I}$ if $(\mathbf{c}_\alpha - \mathbf{V}_b) \cdot (0,1) < 0$ for the bottom wall with a moving velocity $\mathbf{V}_b = (u_b, v_b)$. However, we note that the knowledge of surface normal is not mandatory in the actual implementation. By using the cutting-cell mesh technique, it is possible to distinguish these three types by judging whether a particle will enter into wall or not. Thus, the algorithm at boundary points can be specified according to the boundary types (e.g., the planar type shown in Figure 1 and the two corners shown in Figure 2).

For the D2Q9 lattice, the DR scheme can then be written as

$$f_{\alpha \in \{\mathbf{O}, \mathbf{P}\}}^b = \frac{\sum_{\beta \in \mathbf{I}} f_{\beta}^b}{\sum_{\alpha \in \mathbf{O}} g_{\alpha}^{eq}(\mathbf{V}_b)} g_{\alpha \in \{\mathbf{O}, \mathbf{P}\}}^{eq}(\mathbf{V}_b). \quad (8)$$

The first RHS term can be considered as the fluid density ρ_b at wall obtained according to mass conservation, i.e.,

$$\rho_b = \frac{\sum_{\beta \in \mathbf{I}} f_{\beta}^b}{\sum_{\alpha \in \mathbf{O}} g_{\alpha}^{eq}(\mathbf{V}_b)}. \quad (9)$$

At the bottom wall boundary, the group \mathbf{I} includes discrete velocities $\{7,4,8\}$, $\mathbf{O} \{6,2,5\}$ and $\mathbf{P} \{0,1,3\}$. Due to the exact advection associated with the particle nature of the lattice Boltzmann algorithm, we can calculate the mass of particles cross the boundary by using the distribution function instead of flux terms, see also [21]. For single speed lattices including the D2Q9 lattice, it is also mathematically obvious, cf. Eq. (11) in [12].

It is straightforward to write down the formulations for other planar boundaries. Corners are slightly more complicated. For instance, as shown in Figure 2, discrete velocities $\{1,2,5\}$ can be considered as the group \mathbf{I} , $\{3,4,7\}$ as the group \mathbf{O} and $\{0,6,8\}$ as the group \mathbf{P} . Thus, we can use the rule (8) implement the boundary scheme.

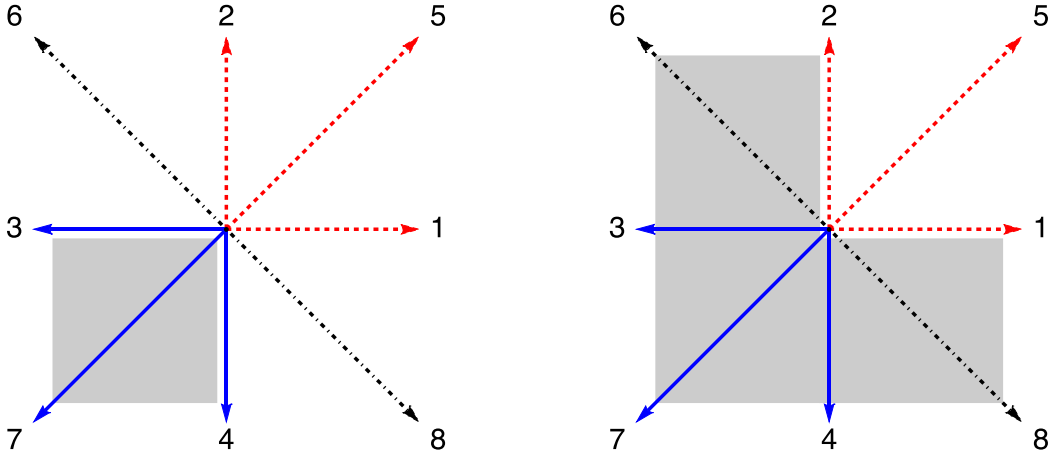


Figure 2 Schematic of two types of wall boundary corners. Wall is illustrated by using gray shading. The discrete velocities are categorized into incoming (blue solid lines), outgoing (red dashed lines), and parallel (black dash-dot lines).

The main idea of the BB scheme is that an incoming particle distribution directing to the wall bounces back into the fluid domain in the opposite direction, and therefore the non-slip boundary is supposed to be enforced. Ladd [1] generalized it for the moving body by using

$$f_{\alpha}^b = f_{\bar{\alpha}}^b + 2w_{\alpha}\rho_b \frac{\mathbf{C}_{\alpha} \cdot \mathbf{V}_b}{\theta_0}, \quad (10)$$

which relates the unknown incoming f_{α}^b to its known counterpart $f_{\bar{\alpha}}^b$ with opposite discrete velocity (i.e., $\mathbf{C}_{\bar{\alpha}} = -\mathbf{C}_{\alpha}$) and a simple modification for specifying boundary velocity. For the specific D2Q9 lattice and the bottom wall boundary, we can accordingly treat the discrete velocity pair from the group \mathbf{O} and the group \mathbf{I} respectively. However, as discussed in [7], there is no definition for those in group \mathbf{P} .

It is known that the DR boundary scheme will produce slip velocity at the wall with finite Knudsen number. At the limit of $Kn \rightarrow 0$, the slip velocity will naturally vanish, which can be easily seen from the slip velocity boundary formula. Therefore, according to Eq. (8), $f_\alpha^b = \rho_b g_\alpha^{eq}(\mathbf{V}_b)$ for $\alpha \in \{\mathbf{O}, \mathbf{P}\}$. Moreover, at such limit, the fluid is always in the local equilibrium, i.e., $f_{\beta \in \{I\}}^b = \rho_b g_\beta^{eq}(\mathbf{V}_b)$ for $\beta \in \{I\}$. We note that two groups of equilibrium distribution must adopt the same density since discontinuities must be removed by the very fast particles collisions. Noticing the fact that for a pair of discrete velocities \mathbf{C}_α and $\mathbf{C}_{\bar{\alpha}} = -\mathbf{C}_\alpha$, we have

$$\rho_b g_\alpha^{eq}(\mathbf{V}_b) = \rho_b g_{\bar{\alpha}}^{eq}(\mathbf{V}_b) + 2w_\alpha \rho_b \frac{\mathbf{C}_\alpha \cdot \mathbf{V}_b}{\theta_0}, \quad (11)$$

which can be easily obtained by substituting velocities \mathbf{C}_α and $\mathbf{C}_{\bar{\alpha}}$ into Eq. (2). Thus, we immediately obtain the relation presented in Eq. (10), and we can conclude that, at the limit of $Kn \rightarrow 0$, the DR scheme reduces to the BB scheme for discrete velocity pairs in the groups \mathbf{I} and \mathbf{O} .

The observation above presents an interesting foundation for the BB boundary condition, in particular for the moving boundary. That is, the BB scheme assembles the limiting behavior of the DR scheme. The observation is also consistent with the finding in [6], the non-physical slip velocity will reduce with decreasing the Knudsen number since the distribution functions for discrete velocities in the group \mathbf{P} become closer to equilibrium functions and will naturally cancel each other.

To remove the slip velocity, it is now possible to force the DR scheme working its continuum limit. For a pair of \mathbf{C}_α and $\mathbf{C}_{\bar{\alpha}}$, we directly apply the rule (10) rather than the rule (8)

$$f_\alpha^b = f_{\bar{\alpha}}^b + 2w_\alpha \rho_b \frac{\mathbf{C}_\alpha \cdot \mathbf{V}_b}{\theta_0} \text{ for } \alpha \in \mathbf{O} \text{ and } \bar{\alpha} \in \mathbf{I}, \quad (12)$$

and, for the discrete velocity in the group \mathbf{P} , we apply

$$f_{\alpha \in \{\mathbf{P}\}}^b = \rho_b g_{\alpha \in \{\mathbf{P}\}}^{eq}(\mathbf{V}_b). \quad (13)$$

The rule (12) will force the DR scheme working at the equilibrium mode (i.e., $Kn \rightarrow 0$), and eliminate the slip velocity. Thus, we call it the **equilibrium diffuse reflection (EDR)** scheme. In comparison to the BB scheme, the rule (13) helps to eliminate the ambiguous definition for the discrete velocities in the group \mathbf{P} . Using the rules (12) and (13), it is easy to verify that

$$\sum_{\alpha \in \{\mathbf{O}\}} f_\alpha^b \mathbf{C}_\alpha + \sum_{\beta \in \{I\}} f_\beta^b \mathbf{C}_\beta + \sum_{\gamma \in \{\mathbf{P}\}} f_\gamma^b \mathbf{C}_\gamma \equiv \rho_b \mathbf{V}_b,$$

so that the non-slip boundary condition is exactly implemented.

We also need to alter the rule (9) of ρ_b for the EDR scheme. It is inconsistent with the rule (12) and may produce density discontinuities at boundary according to our experience. For this purpose, we first write the local mass conservation as

$$\sum_{\alpha \in \{\mathbf{O}\}} f_\alpha^b + \sum_{\beta \in \{I\}} f_\beta^b + \sum_{\gamma \in \{\mathbf{P}\}} f_\gamma^b = \rho_b. \quad (14)$$

Substituting the rules (12) and (13) into Eq. (14), the only unknown quantity is the density ρ_b which can be solved accordingly. For instance, the formulations at the boundary points shown in Figure 1 and Figure 2 can be calculated out as

$$\rho_b = \frac{6(f_4 + f_7 + f_8)\theta_0}{\theta_0 + v_b^2 - \sqrt{3\theta_0}v_b},$$

and

$$\rho_b = \frac{36(f_3 + f_4 + f_7)\theta_0}{9\theta_0 + 3u_b^2 - 5\sqrt{3\theta_0}u_b + 3u_bv_b + 3v_b^2 - 5\sqrt{3\theta_0}v_b}$$

respectively. The other planar boundaries and boundary corners can be treated straightforward using the same way. In above discussions, we are using physical units so that the reference temperature θ_0 is always presented. For the transformation to lattice units, one may refer to [15] for detail.

4. Numerical validations for equilibrium diffuse reflection scheme

In the following we will conduct numerical validations for three typical benchmark problems. The EDR scheme is implemented into the backend code for the HiLeMMS system within the DL_MESO package, and all simulations are run by using this code.

The first benchmark is the classical two-dimensional pressure-driven channel flow where the top wall is in motion. The channel length and height are set to be L and H respectively, and we set the ratio $L/H = 100$. The pressure difference is set to be $0.00005 \rho_0 \theta_0$ and the pressure at the outlet is set to be $\rho_0 \theta_0$. The fluid viscosity is $0.0017 \rho_0 \sqrt{\theta_0} H$. The velocity of the top wall is $(0.00001 \sqrt{\theta_0}, 0)$. For this configuration, the density at the outlet ρ_0 is chosen as the reference density and the wall temperature θ_0 as the reference temperature. Therefore, the corresponding Knudsen number is 0.0017 if using the channel height is the reference length. In [15], there is a detail discussion on the transformation between various physical or lattice units, we will ignore the detail here.

The pressure profiles at the inlet and outlet are specified using a first-order extrapolation scheme which is implemented in the way described in, e.g., [22]. The wall boundary is enforced in the way described by the rules (12) and (13). For corner points, the pressure inlet/outlet boundary are employed accordingly.

The numerical results (see the left part of Figure 3) agree well with the analytical solution of the NS equations, even using a mesh of 1000×10 cells. It is also observed that there is no non-physical slip velocity at the wall boundary nodes.

The numerical accuracy is measured for the stream-wise velocity component along the vertical centerline of the channel by conducting four simulations with 5, 10, 20, and 40 cell at the vertical (Y) direction. The errors are calculated against the analytical solution by using the L^2 norm for a vector ϕ , i.e.,

$$E = \frac{\|\phi - \phi_R\|_2}{\|\phi_R\|_2}. \quad (15)$$

where $\|\phi\|_2 = \sqrt{\phi_1^2 + \dots + \phi_n^2}$ and the reference solution is denoted by ϕ_R . In this case, we consider the velocities at the six grid points specified by the simulations with five cells. The results in the right part of Figure 3 shows accuracy slightly better than the second order. Since there is no slip velocity at wall boundary, no error is introduced into bulk solution and we expect the second accuracy of Eq. (7).

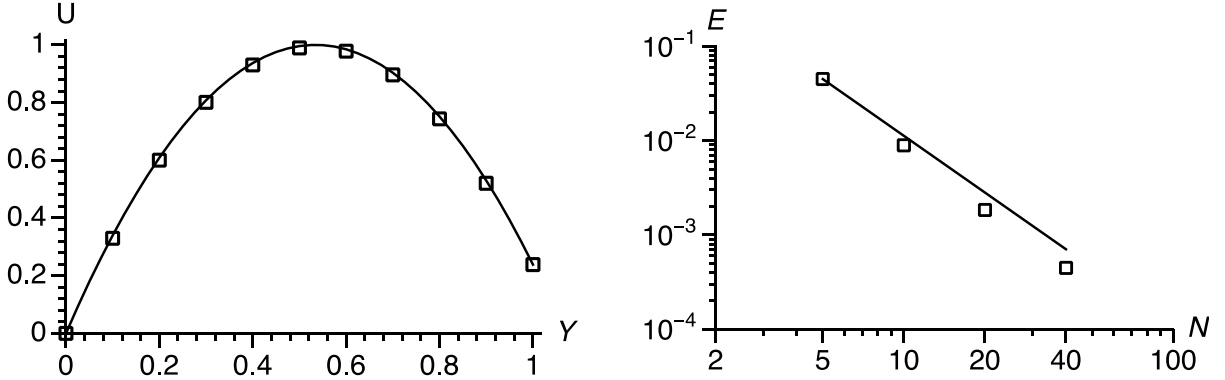


Figure 3 (Left) Profiles of stream-wise velocity component. The analytical solution is shown as the solid line. The speed is normalized by its maximum; (Right) Numerical accuracy. The ideal slope (-2) is shown using the solid line.

The second case is the lid-driven cavity flow, where we keep the lid speed as $0.1\sqrt{\theta_0}$ and again the wall temperature is considered as the reference temperature. To validate the boundary condition, we simulate three Re numbers i.e., 100, 400 and 1000. By using 256×256 cells, we compare the solutions with those in [23]. As has been shown in Figure 4, the results agree well with each other, and importantly, there is again no non-physical slip velocity at wall boundaries.

For the last validation, we consider a channel flow around a square cylinder at $Re = 25$ defined by the square width D and the average velocity at the inlet. The channel length is set to be $L = 15D$ and height $H = 2.5D$. The left bottom corner of the square is located at the point $(4D, 0.75D)$, see Figure 6. At the inlet, we enforce a uniform velocity profile $(0.05\sqrt{\theta_0}, 0)$ by using the proposed EDR formulation. For the outlet, we use the first-order extrapolation scheme to set a uniform pressure (density) profile ρ_0 , i.e., the reference density. Therefore, the viscosity is $0.002 \rho_0 \sqrt{\theta_0} D$ and the Knudsen number is 0.002.

The proper simulation is conducted by using 900×150 cells, and the results are compared to those given by an in-house multi-block Navier-Stokes (NS) solver, THOR, in which the finite volume approach has been employed. The diffusive and source terms are discretized by a central difference scheme and the QUICK scheme [24] is employed for the convective terms. A collocated grid arrangement is used and the interpolation scheme of Rhie and Chow [25] is employed to eliminate any non-physical pressure oscillations in THOR. For the purpose of comparison, we use the same mesh for both solvers. In Figure 5, it is found that two solvers agree well with each other. In both corners and planar walls, the zero speed is correctly enforced. In Figure 6, it shows that the flow features are correctly captured. In the LB predictions, the stagnation point is located at $5.959D$ while the NS solver gives $5.947D$, the relative error is within 1.3%.

We also test the stability for this flow by using 60×10 cells, which means only 4 cells are distributed on the square. The Reynolds number is adjusted while the inlet velocity is set to be $(0.005\sqrt{\theta_0}, 0)$ and the outlet pressure is also $\rho_0\theta_0$. It is found that the stable simulation can be maintained where $Re = 250$, $Kn = 0.00002$ and the relaxation time in the lattice unit is 0.500866, which demonstrates satisfactory stability. Here a “stable” simulation means that

the simulation lasts at least 300000 time steps without the occurrence of “NAN” and afterwards we stop monitoring.

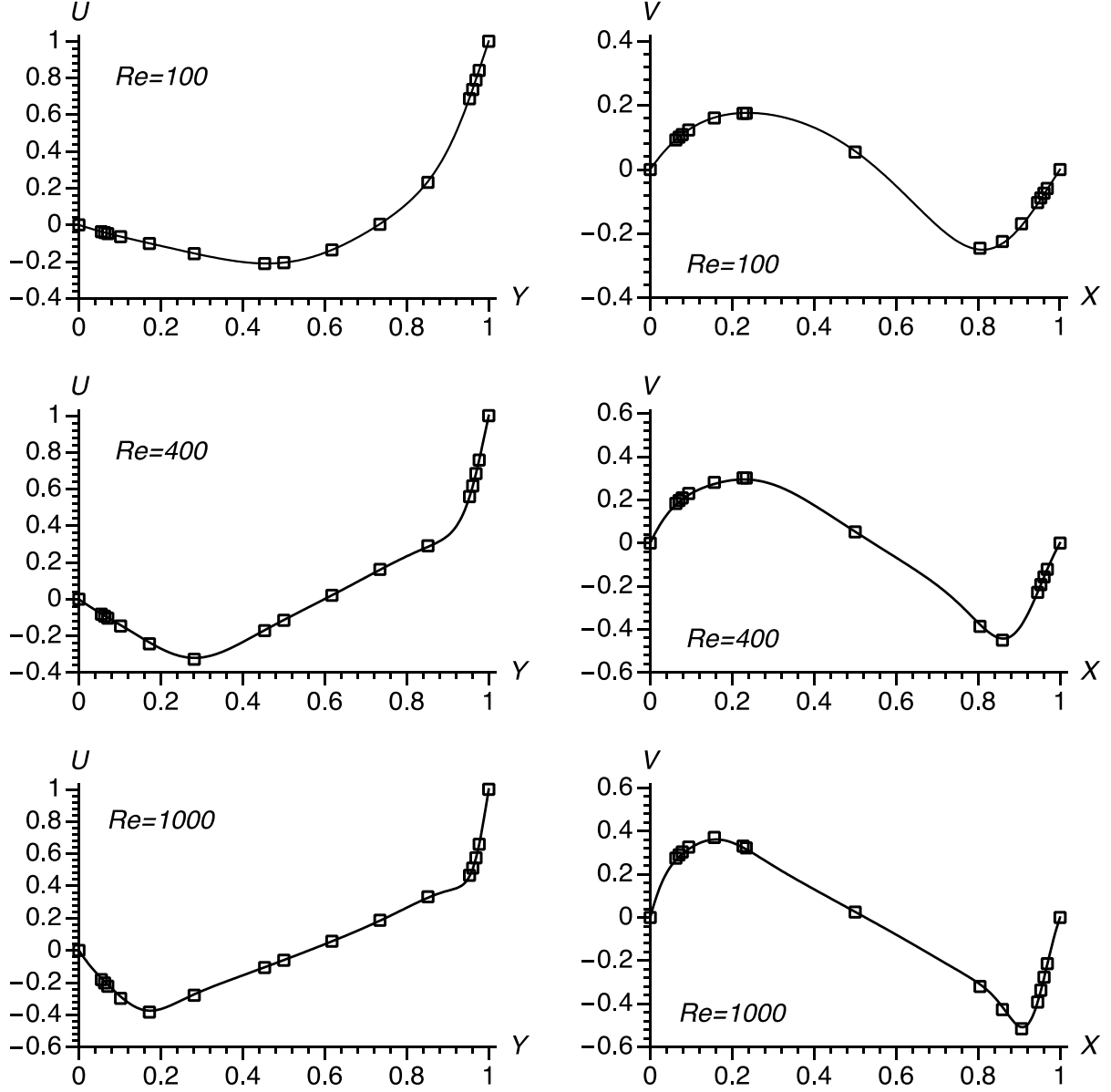


Figure 4 Profiles of horizontal (vertical) velocity component through the vertical (horizontal) centerline of the cavity. The horizontal and vertical components are normalized by the lid speed, which is set to be $0.1 \sqrt{\theta_0}$ for all three cases. The benchmark solutions are taken from Ghia et al [23].

4. Concluding remarks

By analyzing the limiting behavior of the DR boundary scheme at $Kn \rightarrow 0$, we have found that the commonly used BB boundary scheme is an incomplete form of the DR scheme, where the missing definition for the discrete velocities in the group \mathbf{P} induces the well-known non-physical slip velocity [7]. Utilizing this fact, we suggest the EDR scheme to implement the nonslip boundary condition, which forces the DR scheme working at its equilibrium limit. To

validate the scheme, numerical simulations are conducted for the pressure-driven channel flow, the lid-driven cavity flow and the channel flow around a square cylinder, and satisfactory results are observed. We also note that the EDR scheme requires no extra effort in the implementation in comparison to the BB scheme although it could induce more computational overhead due to the calculation of the equilibrium function for the discrete velocities in the group P . Although the validations are conducted for two-dimensional flows with boundaries aligned to grid lines in this work for avoiding error induced by geometry, the EDR scheme, i.e., Eqs. (12), (13) and (14), can be applied to three-dimensional problems or curved boundary since there are only minor modifications in comparison to the BB scheme, i.e., Eq. (13). In fact, we have presented treatments for the corners shown in Figure 2, which are ready for two-dimensional curved boundaries. Nevertheless, directly applying the scheme to zig-zag stairs will be subject to the geometry error, and we will investigate possible ways of improving accuracy in the near future, e.g., combining with spatial interpolations [26].

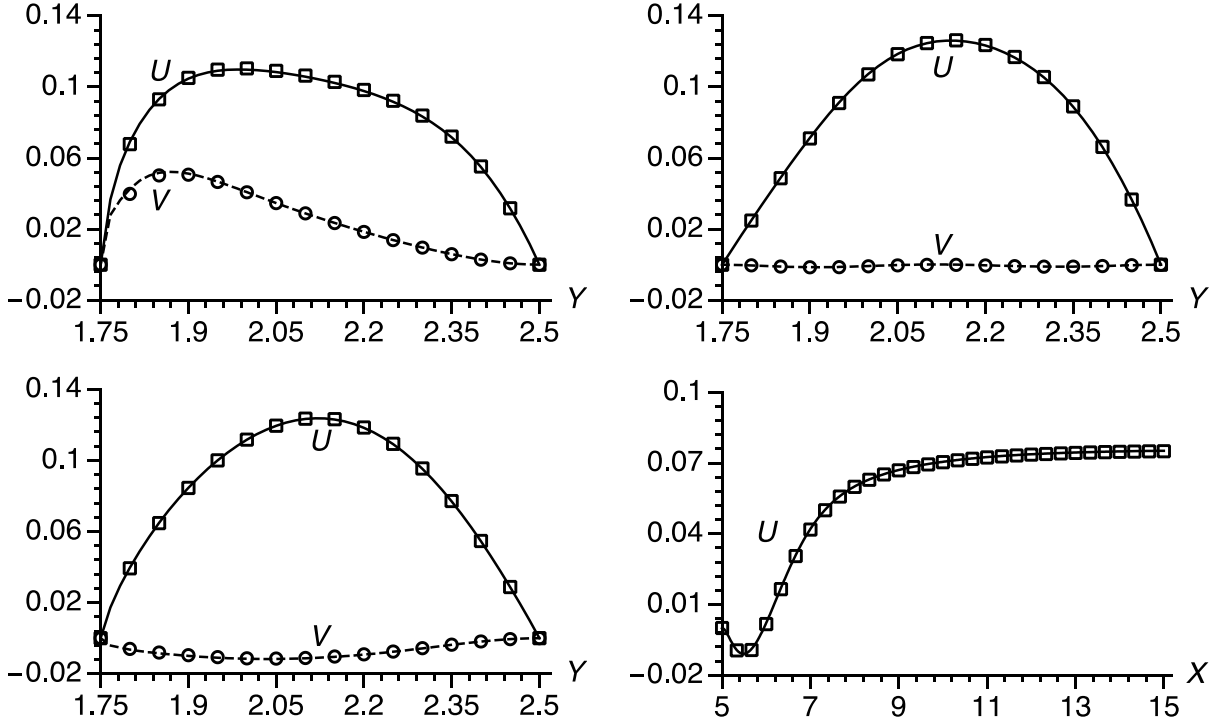


Figure 5 Velocity profiles along: (Top left) the vertical line from the top left corner of the square to the top wall of the channel; (Top right) the vertical line from the middle point of top wall of the square to the top wall of the channel; (Bottom left) the vertical line from the top right corner of the square to the top wall of channel; (Bottom right) the horizontal line of the channel after the square. The symbols are the results of LB simulations with the proposed boundary conditions.

Acknowledgements

We gratefully acknowledge support from EPSRC under grants EP/N016602/1(DRE), EP/L00030X/1, EP/P022243/1 and EP/N033841/1 (JPM and DRE). We also thank the Royal Society (UK) and NSFC (China) for their support on bilateral visiting.

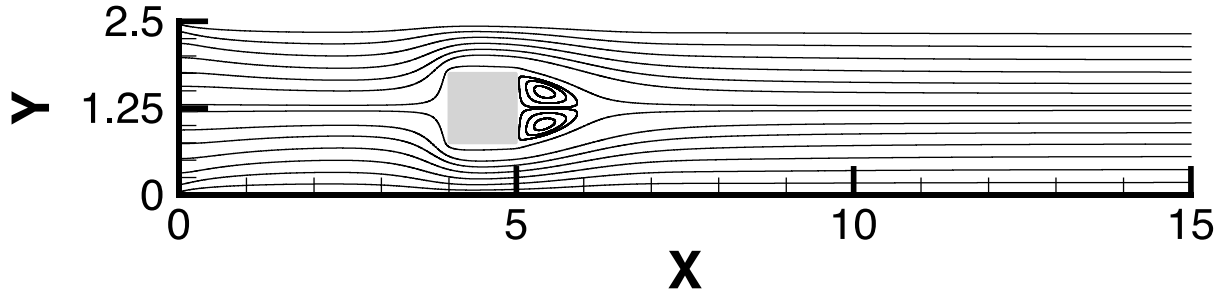


Figure 6 Streamline plot of the flow around a square cylinder at $Re = 25$.

References

- [1] A. J. C. Ladd, *J. Fluid Mech.* **271**, 285 (1994).
- [2] X. He, Q. Zou, L.-S. Luo, and M. Dembo, *J. Stat. Phys.* **87**, 115 (1997).
- [3] R. Cornubert, D. D'Humières, and D. Levermore, *Phys. D* **47**, 241 (1991).
- [4] L.-S. Luo, W. Liao, X. Chen, Y. Peng, and W. Zhang, *Phys. Rev. E* **83**, 1 (2011).
- [5] C. Pan, L.-S. Luo, and C. T. Miller, *Comput. Fluids* **35**, 898 (2006).
- [6] P. Prestininzi, A. Montessori, M. La Rocca, and S. Succi, *Int. J. Mod. Phys. C* **27**, 1650037 (2016).
- [7] J. Meng, X.-J. Gu, and D. R. Emerson, *J. Comput. Sci.* (2017).
- [8] S. Chikatamarla and I. Karlin, *Phys. Rev. E* **79**, 1 (2009).
- [9] X. Shan, *Phys. Rev. E* **81**, 1 (2010).
- [10] J. Clerk Maxwell, *Phil Trans R Soc Lond* **170**, 231 (1879).
- [11] R. Gatignol, *Phys. Fluids* **20**, 2022 (1977).
- [12] S. Ansumali and I. V. Karlin, *Phys. Rev. E* **66**, 026311 (2002).
- [13] J. Meng and Y. Zhang, *J. Comput. Phys.* **230**, 835 (2011).
- [14] J. Meng, Y. Zhang, N. G. Hadjiconstantinou, G. A. Radtke, and X. Shan, *J. Fluid Mech.* **718**, 347 (2013).
- [15] K. Hu, J. Meng, H. Zhang, X.-J. Gu, D. R. Emerson, and Y. Zhang, *Comput. Fluids* **156**, 1 (2017).
- [16] Y. H. Qian, D. D'Humieres, and P. Lallemand, *EPL Europhys. Lett.* **17**, 479 (1992).
- [17] X. He and L.-S. Luo, *Phys Rev E* **56**, 6811 (1997).
- [18] S. Ansumali, I. Karlin, and H. Öttinger, *EPL Europhys. Lett.* **63**, 798 (2003).
- [19] X. W. Shan, X. F. Yuan, and H. D. Chen, *J. Fluid Mech.* **550**, 413 (2006).
- [20] X. He, S. Chen, and G. D. Doolen, *J Comput Phys* **146**, 282 (1998).
- [21] J. Meng and Y. Zhang, *J. Comput. Phys.* **258**, 601 (2014).
- [22] F. Verhaeghe, L. Luo, and B. Blanpain, *J. Comput. Phys.* **228**, 147 (2009).
- [23] U. Ghia, K. N. Ghia, and C. T. Shin, *J. Comput. Phys.* **48**, 387 (1982).
- [24] B. P. Leonard, *Comput. Methods Appl. Mech. Eng.* **19**, 59 (1979).
- [25] C. M. Rhie and W. L. Chow, *AIAA J.* **21**, 1525 (1983).
- [26] M. Bouzidi, M. Firdaouss, and P. Lallemand, *Phys. Fluids* **13**, 3452 (2001).